PROCEEDINGS OF SPIE

SPIEDigitalLibrary.org/conference-proceedings-of-spie

# Hyperspectral imaging for intraoperative diagnosis of colon cancer metastasis in a liver

Ivica Kopriva, Gorana Aralica, Marijana Popović Hadžija, Mirko Hadžija, Laura-Isabelle Dion-Bertrand, et al.

Ivica Kopriva, Gorana Aralica, Marijana Popović Hadžija, Mirko Hadžija, Laura-Isabelle Dion-Bertrand, Xinjian Chen, "Hyperspectral imaging for intraoperative diagnosis of colon cancer metastasis in a liver ," Proc. SPIE 10956, Medical Imaging 2019: Digital Pathology, 109560S (18 March 2019); doi: 10.1117/12.2503907

SPIE.

Event: SPIE Medical Imaging, 2019, San Diego, California, United States

# Hyperspectral imaging for intraoperative diagnosis of colon cancer metastasis in a liver

Ivica Kopriva[1*], Gorana Aralica[2, 3] Marijana Popović Hadžija[4], Mirko Hadžija[4], Laura-Isabelle Dion-Bertrand[5] and Xinjian Chen[6]

[1]Division of Electronics, Ruđer Bošković Institute, Bijenička cesta 54, P.O. Box 180, 10002, Zagreb, Croatia
[2]Department of Pathology and Cytology, Clinical Hospital Dubrava, Avenija Gojka Šuška 6, 10000 Zagreb, Croatia
[3]School of Medicine, University of Zagreb, Šalata 3, 10000 Zagreb, Croatia
[4]Division of Molecular Medicine, Ruđer Bošković Institute, Bijenička cesta 54, 10000 Zagreb, Croatia
[5]Photon etc., 5795 De Gaspe Avenue, Montreal, QC, H2S 2X3, Canada
[6]School of Electronic and Information Engineering, Soochow University, Suzhou 215123, China

e-mail: ikopriva@irb.hr, garalica@kbd.hr, Marijana.Popovic.Hadzija@irb.hr, Mirko.Hadzija@irb.hr, lidion.bertrand@photonetc.com, xjchen@suda.edu.cn

**Abstract**

Hyperspectral imaging (HSI) is being shown as an emerging modality with a great potential in disease diagnosis and surgical cancer resection. Herein, we evaluate feasibility of the HSI to discriminate and diagnose colon cancer metastasis in a liver from five hematoxylin and eosin stained histopathological specimens. They were collected from the same patient during intraoperative frozen section analysis. Cancer and non-cancer spectra along with corresponding spatial maps were estimated from hyperspectral images by means of spectral unmixing. It was found that maximal angle between cancer spectra is 1.02 degrees less than minimal angle between cancer vs. non-cancer spectra. Thus, spectrum angle mapper was used for pixel-based diagnosis of cancer yielding sensitivity between 81.23% and 97.12%, specificity between 85.85% and 97.3%, and accuracy between 86.85% and 96.92%.

**Keywords:** intraoperative diagnosis, hyperspectral microscopic imaging, liver, colon cancer metastasis, spectral angle mapper.

## 1 INTRODUCTION

Hyperspectral imaging (HSI), also called imaging spectroscopy, produces images up to several hundreds of adjacent spectral bands [1]. HSI systems, originated from remote sensing, were used for military needs and explored for various applications by NASA [2]. With the appearance of commercial airborne HSI systems new applications in resource management, agriculture, mineral

Medical Imaging 2019: Digital Pathology, edited by John E. Tomaszewski, Aaron D. Ward,
Proc. of SPIE Vol. 10956, 109560S · © 2019 SPIE · CCC code:
1605-7422/19/$18 · doi: 10.1117/12.2503907

exploration and environmental monitoring have emerged [3]. HSI is also an emerging modality for medical applications, especially in disease diagnosis and image-guided surgery [4]. HSI acquires three-dimensional dataset, called image cube, with two spatial dimensions and one spectral dimension. Upon assumption that physical properties of tissue such as absorption, fluorescence and scattering change during progressions of disease, [5], acquired hyperspectral image carries quantitative information about tissue pathology [6, 7]. Thus, spectra associated with specific tissues can serve as basis for disease screening, detection and diagnosis [4]. In particular, HSI has demonstrated great potential in diagnosis of cancer in the cervix [6, 8], breast [9, 10], colon [11-14], head and neck [15], prostate [16], ovary [17] and lymph nodes [18], to name a few. For more in depth coverage of the use of HSI in diagnosis of various diseases we refer interested reader to [4]. The aim of the present study was to evaluate feasibility of the HSI to discriminate and diagnose colon cancer metastasis in a liver from five hematoxylin and eosin (H&E) stained specimens. They were collected from the same patient during intraoperative frozen section analysis. Spectral unmixing [19, 20], was applied on recorded hyperspectral images yielding pixel-based decomposition into spectra of pure tissues and fractional abundances that indicate spatial maps of pure tissues. Pathologist identified spatial maps associated with metastasis of colon cancer. Consequently, corresponding spectra were identified as spectra of metastasis of colon cancer. Afterwards, maximal angle between cancer spectra and minimal angle between cancer spectra and spectra of non-cancer tissues were calculated yielding a gap in the amount of 1.02 degrees. Thus, angular threshold was defined for pixel-based spectral angle mapper (SAM) diagnosis. Afterwards, the angle between the reference cancer spectra, obtained as average of cancer spectra, and spectra of each pixel was calculated and compared with the threshold, whereas pixels with angles less than the threshold were diagnosed as cancerous. That pixel-based diagnosis enabled quantification of diagnostic performance. Thereby, spatial maps obtained through spectral unmixing, and identified by pathologist as metastasis of colon cancer, served as ground truth necessary to estimate sensitivity, specificity, accuracy and Dice coefficient (DC). The rest of this paper is organized as follows. Sec. 2 presents details related to the collection and preparation of the specimen, hyperspectral image acquisition, identification of cancer spectra by means of spectral unmixing and patholgist' identification of cancer spatial maps. Design of spectral angle mapper (SAM) classifier for pixel-based diagnosis is also presented in Sec. 2. Quantification of the performance of the SAM pixel-based diagnosis is presented in Sec. 3. Discussion and conclusions are given in Sec. 4.

## 2 MATERIALS AND METHODS

### 2.1 Ethics statement

This study was approved by the Ethics Committee of the Clinical Hospital Dubrava (May 24, 2016).

### 2.2 Samples of human liver tissue and color RGB image acquisition

H&E stained frozen sections of liver with metastasis of colon cancer were collected during intraoperative surgery procedure in Clinical Hospital Dubrava, Zagreb, Croatia. RGB color images

of H&E stained specimens were acquired on light microscope Olympus BX51 with a DP50 camera, Japan, and magnification 400x.

### 2.3 Immunohistochemical staining

To confirm diagnosis, paraffin-embedded sections were immunohistochemically stained to CDX2 antigene, a diagnostic marker for colorectal differentiation. Primary antibody CDX2 clone DAK-CDX2 (product No. M3636) and Dako Envision System (Denmark) were used. RGB images of stained specimens were acquired under light microscope Olympus BX51 with a DP50 camera, Japan, magnification 400x, Figure 1.

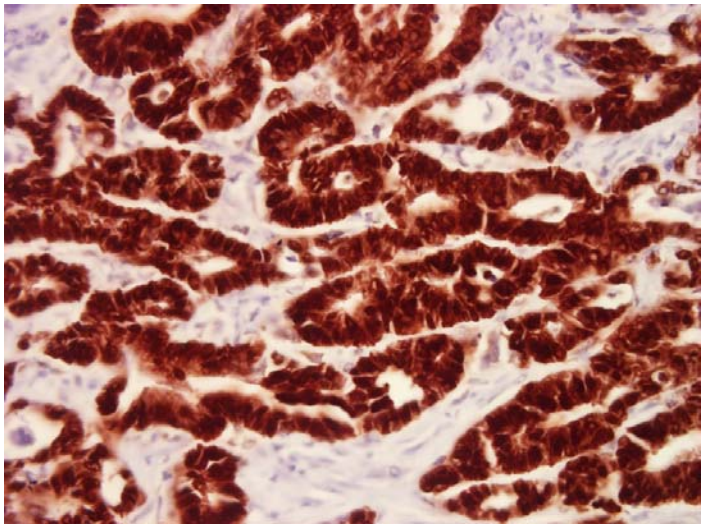

**Figure 1.** The light microscope acquired RGB color image of the CDX2 stained specimen. Colon cancer metastasis positive to CDX2 are colored brown and that confirms diagnosis of metastasis of colon cancer in a liver.

### 2.4 Hyperspectral microscopic image acquisition

Images of the regions of interest marked on H&E stained histopathological specimens were acquired with Photon etc's hyperspectral fluorescence microscope IMA [21, 22]. IMA uses volume Bragg gratings (VBG) to acquire spectrally resolved images combined into a data cube. VBG allows global imaging, a method where the signal coming from every point in the field of view is simultaneously collected avoiding x-y or line scanning. The data cubes are composed of 351 gray scale images recorded at 1 nm spectral resolution (ranging from 450 nm to 800 nm) with focus at 590 nm. Each gray scale image comprised of 1392x1040 pixels with a spatial resolution of 1 μm, the images were acquired with a 20X objective. Figure 2 shows grayscale intensity images of selected wavelengths from the HSI of H&E stained specimen of liver with colon cancer metastasis.

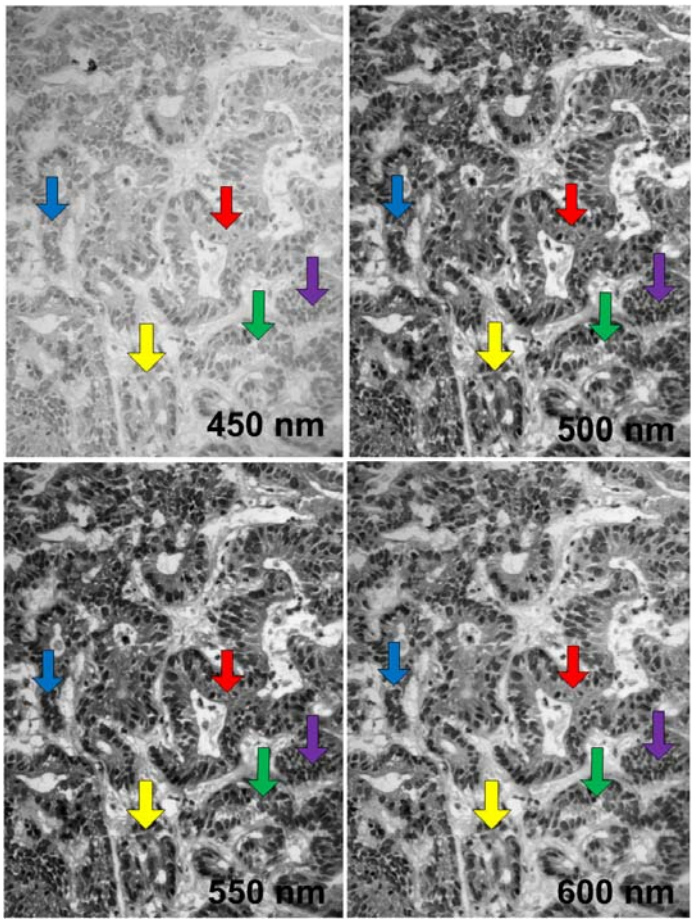


**Figure 2.** Gray scale intensity images at specified wavelengths as parts of hyperspectral image cube of H&E stained specimen of human liver with metastasis of colon cancer. Corresponding cancer patterns are denoted in each image by an arrow of the same color.

### 2.5 Spectral unmixing

Prior to spectral unmixing the hyperspectral image cube $\underline{\mathbf{X}} \in \mathbb{R}_{0+}^{1392\times1040\times351}$ comprised of 351 spectral images with the size of 1392×1040 pixels is unfolded into a matrix $\mathbf{X} \in \mathbb{R}_{0+}^{351\times(1392\times1040)}$ The spectrum of each pixel $\mathbf{x}_p \in \mathbb{R}_{0+}^{351\times1}$, $p$=1,.., 1392×1040, is well approximated by linear mixture of distinct tissues spectra weighted by corresponding abundances [19, 20]:

$$\mathbf{x}_p = \sum_{j=1}^{J} \mathbf{m}_j s_{jp} \quad \forall p = 1,..., I_1 \times I_2 \tag{1}$$

where $\mathbf{m}_j \in \mathbb{R}_{0+}^{351\times1}$ stands for pure spectra of the $j$th tissue, $J$ stands for overall number of tissues, and abundance $s_{jp}$ stands for percentage of pure tissue $j$ that is present in the pixel $p$. In the presents

study $J$ was set to 6. Thus, it was assumed that number of distinct tissues present in the field of view of the hyperspectral microscope does not exceed 6. Due to the nature of the problem nonnegativity and sum-to-one constraints are imposed on abundances:

$$\mathbf{s}_p \in S = \left\{ \mathbf{s} \in \mathbb{R}^J \,\middle|\, \mathbf{s} \geq \mathbf{0}, \mathbf{s}^{\mathrm{T}} \mathbf{1} = 1 \right\} \qquad \forall p = 1,...,1392 \times 1040 \tag{2}$$

where $S$ denotes the feasible set of abundance vectors [20]. Provided that pure tissues spectra are estimated accurately, abundances can be obtained by solving constrained least square problem [19, 20, 23]:

$$\hat{\mathbf{s}}_p = \arg\min_{\mathbf{s}_p \in S} \left\| \mathbf{x}_p - \mathbf{M}\mathbf{s}_p \right\|_2^2 \qquad \forall p = 1,...,1392 \times 1040 \tag{3}$$

where $\mathbf{M} \in \mathbb{R}_{0+}^{351 \times 6}$ stands for matrix of pure tissues spectra. Thus, knowledge of $\mathbf{M}$ is of key importance for hyperspectral image analysis. To this end, many state-of-the-art algorithms for estimation of pure spectra rely on pure pixel assumption [24-26]. This assumption implies that each pure spectra is present in at least one pixel alone. Due to 1 μm spatial resolution of the hyperspectral fluorescence microscope the pure pixel assumption is justified experimentally. Thus, algorithms such as N-FINDR, [24], vertex component analysis, [25], and successive volume maximization, [26], employ various pure pixels search strategies to estimate the pure spectra. In the present study NFINDR and fully constrained least square (FCLS), [27], algorithms were used to respectively estimate pure spectra and fractional abundances. To this end, Figure 3 shows spectra and spatial maps of metastasis of colon cancer and five non-cancerous tissues obtained from spectral unmixing of hyperspectral image of one H&E stained specimen. Figure 4(a) shows RGB color image of the same H&E stained specimen recorded by light microscope. Gray scale intensity image acquired by hyperspectral microscope at wavelength of 500 nm is shown in Figure 4(b). Figure 4(c) shows fractional abundance map associated with metastasis of colon cancer. Corresponding cancer patterns are pointed in each picture by arrows of the same color. Based on this information pathologist confirmed the fractional abundance map as the cancer map. The same procedure was used for hyperspectral images of all five specimens. These cancer maps served as ground truth for performance quantification of spectrum angle mapper (SAM) pixel-based diagnosis. Figure 5 shows cancer spectra estimated from five specimens by NFINDR algorithm. The average of these cancer spectra is also shown in Figure 6 and was used for the SAM classifier pixel-based diagnosis.

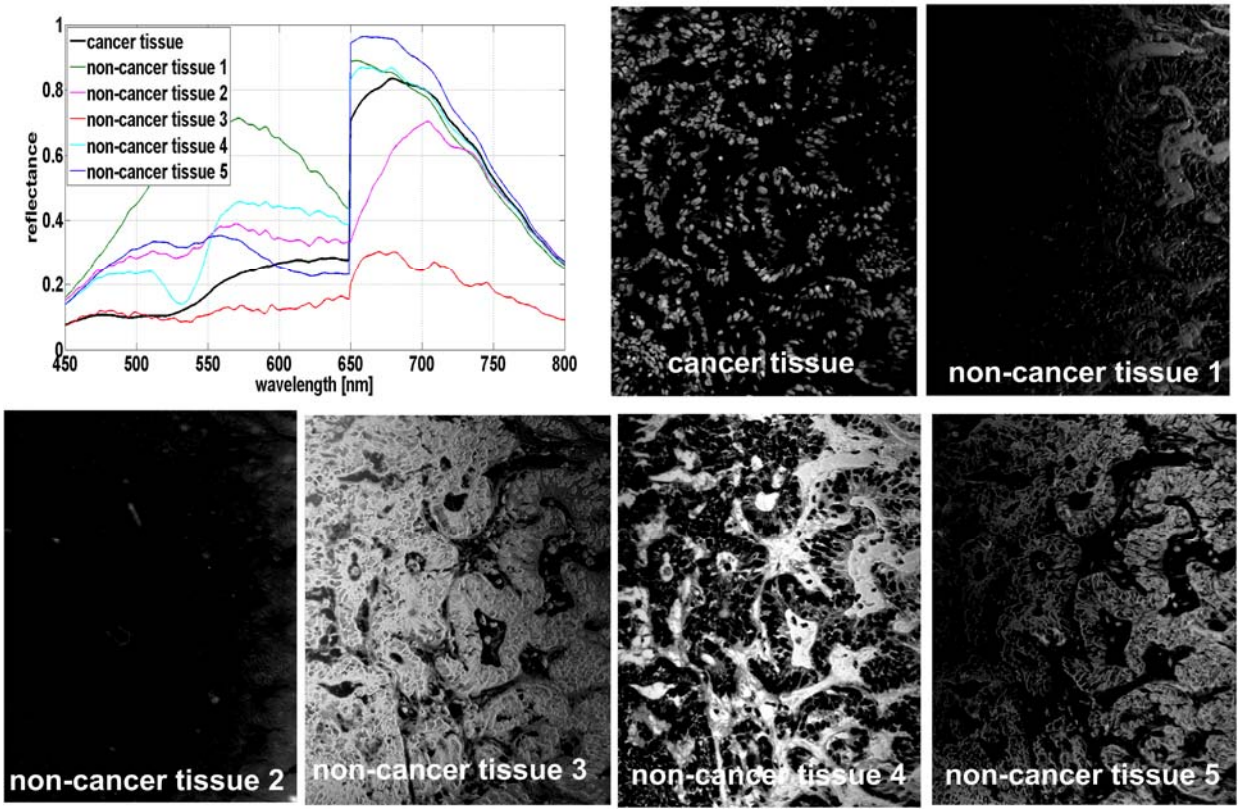


**Figure 3.** Spectra and spatial maps of cancer and non-cancer components obtained by spectral unmixing of the hyperspectral image cube as in Figure 2.

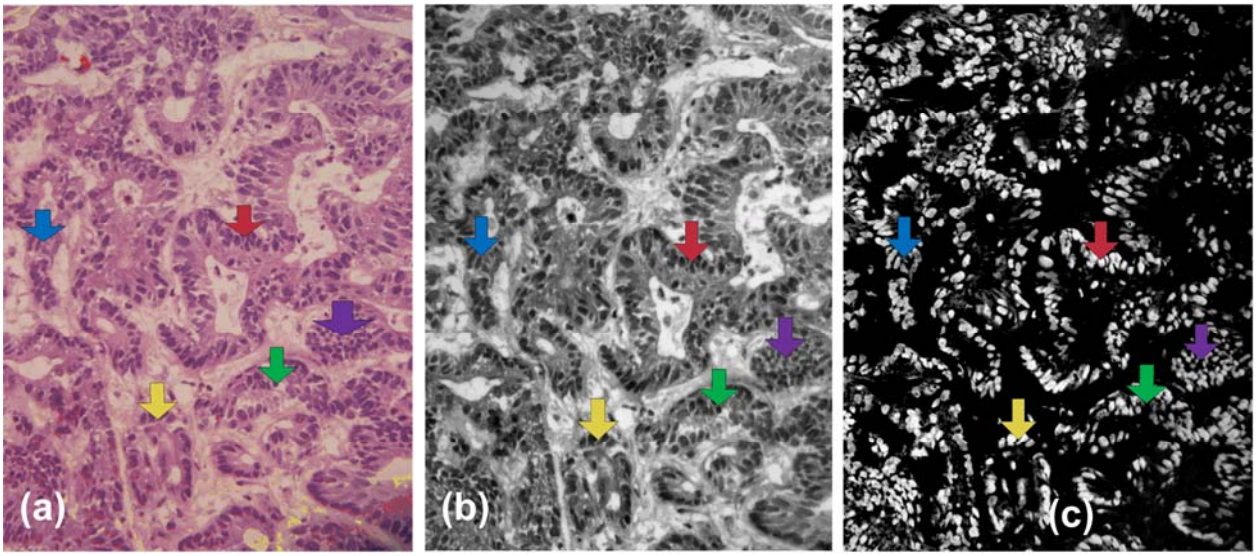


**Figure 4.** Specimen of human liver with metastasis of colon cancer collected during intraoperative surgery procedure: (a) RGB color image of the H&E stained specimen; (b) gray scale intensity image recorded by hyperspectral microscope at 500 nm; (c) fractional abundance map of the cancer estimated by spectral unmixing. Corresponding cancer patterns are denoted in each image by an arrow of the same color.

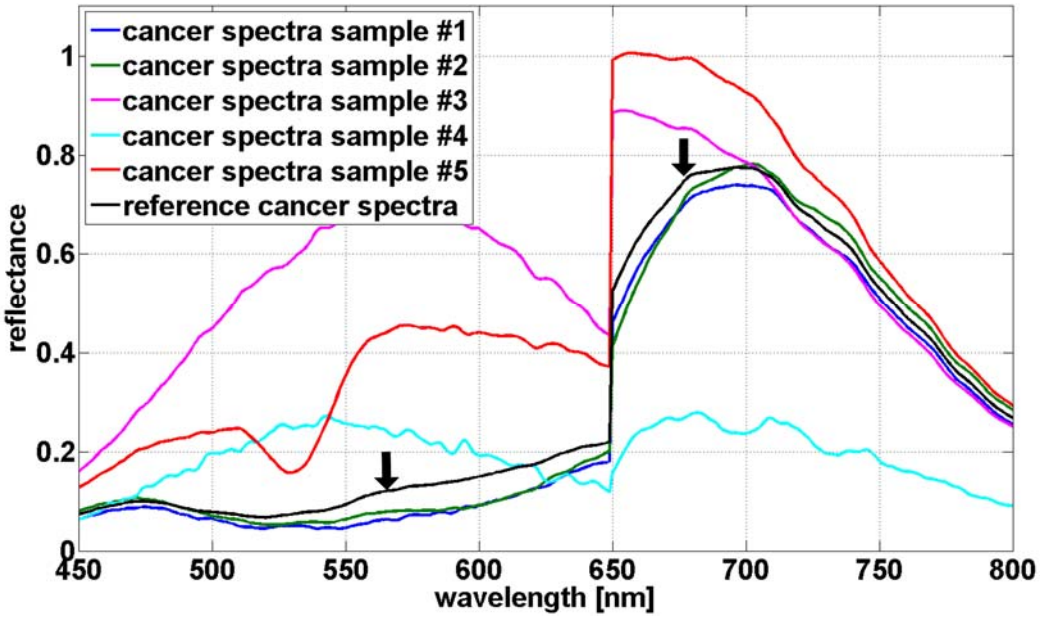


**Figure 5.** Cancer spectra estimated from five specimens by NFINDR algorithm. Reference cancer spectrum (obtained as average of five cancer spectra) is shown in black color and pointed by an arrow.

### 2.6 Spectral angle mapper diagnosis

SAM is supervised pixel-based classifier that compares cancer spectra $\mathbf{x}^c \in \mathbb{R}_{0+}^{351\times 1}$ with the pixel spectra $\mathbf{x}_p$ by calculating angle between the two spectra:

$$\alpha_p = \cos^{-1}\left(\frac{\left\langle \mathbf{x}^c, \mathbf{x}_p \right\rangle}{\left\|\mathbf{x}^c\right\|\left\|\mathbf{x}_p\right\|}\right) \qquad p = 1,...,1392\times 1040 \tag{4}$$

where $\langle \bullet,\bullet \rangle$ denotes the inner product between the two vectors and $\|\bullet\|$ denotes the $\ell_2$-norm of the vector. Diagnosis is established through comparison of $\alpha_p$ with a threshold $\alpha^*$:

$$D\left(\mathbf{x}_p\right) = \begin{cases} \text{cancer} & \text{if} \quad \alpha_p \le \alpha^* \\ \text{non-cancer} & \text{if} \quad \alpha_p > \alpha^* \end{cases} \tag{5}$$

Threshold $\alpha^*$ was set on the basis of the values of maximal angle between the cancer spectra and minimal angle between the cancer and non-cancer spectra: $\alpha^* \in \left[12.32^0, 13.34^0\right]$. To this end, Figure 6 shows spectra of the cancer tissue and non-cancerous tissues estimated by NFINDR algorithm from hyperspectral image of one H&E stained specimen.

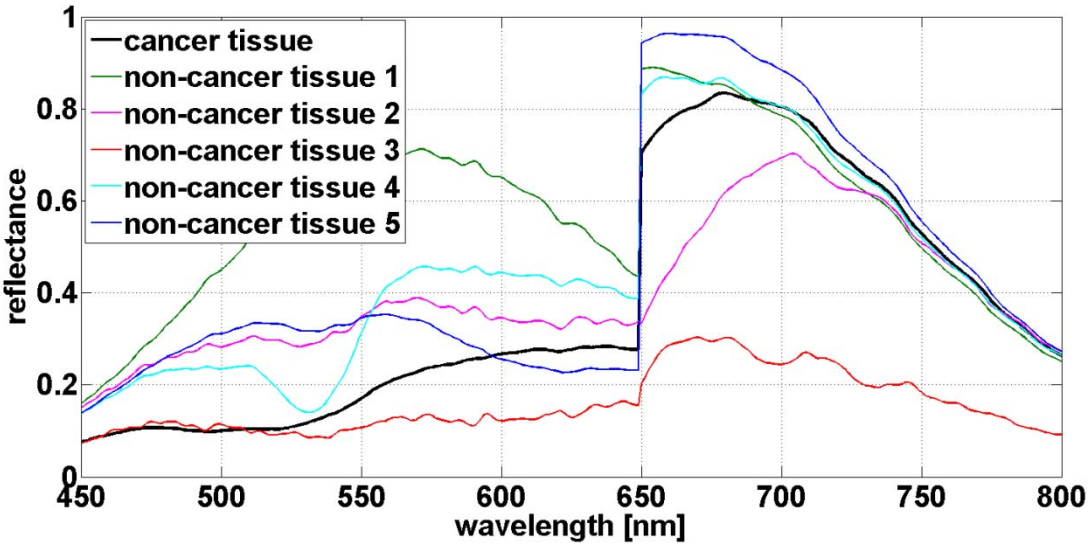


**Figure 6.** Cancer spectrum and spectra of non-cancerous tissues estimated by NFINDR algorithm from the hyperspectral image of H&E stained specimen of human liver with metastasis from colon cancer.

## 3 EXPERIMENTS AND RESULTS

### 3.1 Performance measure

To quantify diagnoses performance we compared fractional abundance maps of the cancer estimated by FCLS algorithm in (3) with pixel-based diagnoses obtained by SAM classifier (4). To this end, sensitivity, specificity, accuracy and DC were estimated for cancer diagnosis for each of the five specimens. All metrics are greater than or equal to 0 and less than or equal to 1. While sensitivity and specificity emphasize respectively errors in diagnoses of cancer or non-cancer pixels, accuracy and DC emphasize errors in diagnoses of both cancer and non-cancer pixels. Figure 7(a) to 7(d) show respectively sensitivity, specificity, accuracy and DC estimated in diagnoses of cancer from five specimens as a function of angular threshold $\alpha^* \in \left\{12.32^0, 12.5^0, 12.83^0, 13^0, 13.2^0\right\}$. In particular, achieved sensitivity is between 81.23% and 97.12%, specificity between 85.85% and 97.3%, accuracy between 86.85% and 96.92% and DC between 0.5971 and 0.9008.

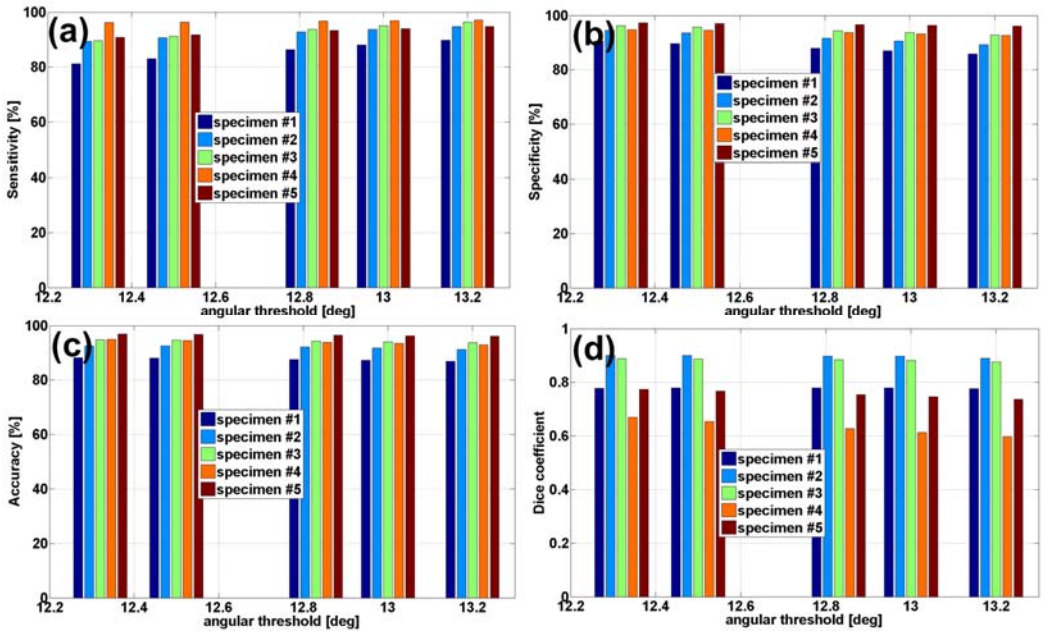


**Figure 7.** Performance measures of SAM classifier pixel-based diagnosis as a function of angular threshold: (a) sensitivity in percentage; (b) specificity in percentage; (c) accuracy in percentage; (d) Dice coefficient (D). For Dice coefficient 0 stands for disagreement between diagnoses and ground truth and 1 stands for perfect agreement between diagnoses and ground truth.

## 4 DISCUSSION AND CONCLUSIONS

The feasibility of the HSI to diagnose metastasis of colon cancer in liver from H&E stained specimens collected during intraoperative frozen section analysis is evaluated. For that purpose spectral unmixing of the acquired hyperspectral images was performed to decompose image of each specimen into spectra of pure tissues and fractional abundances that indicate spatial maps of pure tissues. Cancer related spatial maps were identified by pathologist and served as ground truth for performance assessment of SAM classifier pixel-based diagnoses. Angular threshold for SAM classifier based diagnoses was obtained from the experimentally found gap between maximal angle between cancer spectra and minimal angle between cancer and non-cancer spectra. Estimated sensitivity, specificity and accuracy are above 80%. Thus, it is conjectured capability of HSI modality for diagnosis, screening and image-guided surgery of metastasis of colon cancer in a liver. In the long term it is necessary to investigate possibility to build library of spectra of other types of gastrointestinal cancers. That is necessary in order to verify whether: (*i*) angle between the spectra of the same type of cancer is less than or greater than angle between the spectra of different types of cancer; (*ii*) angle between the spectra of cancers of interest is less than or greater than angle between spectra of cancer and non-cancerous tissues. The outcome of this investigation would confirm or eliminate conjecture that HSI imaging modality is capable for diagnosis, screening and image-guided surgery of cancers. Furthermore, it is also necessary to investigate whether more

advanced spectral unmixing methods, such as the ones based on nonlinear mixture models, can yield estimates of cancer spectra and corresponding spatial maps with smaller variability.

## ACKNOWLEDGEMENTS

This work was supported in part through; grant IP-2016-06-5235 "Structured Decompositions of Empirical Data for Computationally-Assisted Diagnosis of Disease" funded by the Croatian Science Foundation; bilateral Chinese-Croatian project "Structure constrained decompositions for enhancement and segmentation of PET/CT and OCT images" funded by Ministry of Science, Education and Sports Republic of Croatia and Ministry of Science and Technology People's Republic of China; European Regional Development Fund under the grant KK.01.1.1.01.0009 (DATACROSS). We thank Sébastien Desgent for acquisition of the images of H&E stained specimens on hyperspectral microscope.

## REFERENCES

[1] Wolfe, W. L., [Introduction to Imaging Spectrometers], SPIE Press (1997).

[2] Goetz, A. F. H., "Three decades of hyperspectral remote sensing of the Earth: a personal view," Remote Sens. Environ. 113, (Suppl. 1), S5-S16 (2009).

[3] Ma, W. K., Bioucas-Dias, J. M., Chanussot, J., Garder, P., "Signal and image processing in hyperspectral remote sensing," IEEE Sig. Proc. Mag. 31, 22-23 (2014).

[4] Lu, G., Fei, B., "Medical hyperspectral imaging: a review," J. Biomed. Opt., 010901 (2013).

[5] Costas, B., Christos, P., George, E., "Multi/hyper-spectral imaging," in: Boas, D. A., Pitris, C., Ramanujam, N. (Eds.), [Handbook of Biomedical Optics], CRC Press (2011), 131-164.

[6] Ferris, D. G., Dickman, E. D., Holtzapple, N., Miller, J. A., Grogan, A., Bambot, S., "Multimodal hyperspectral imaging for the noninvasive diagnosis of cervical neoplasia," J. Low. Genit. Tract Dis. 5, 65-72 (2001).

[7] Pierce, M. C., Schwarz, R. A., Bhattar, V. S., Mondrik, S., Williams, M. D., Lee, J. J., "Accuracy of in vivo multimodal optical imaging for detection of oral neoplasia," Cancer Prev. Res. 5, 801-809 (2012).

[8] Sidiqqi, A. M., Li, H., Faruque, F., Williams, W., Lai, L., Hughson, M., et al., "Use of hyperspectral imaging to distinguish normal, precancerous, and cancerous cells," Cancer Cytopathol. 114, 13-21 (2008).

[9] Panasyuk, S. V., Yang, S., Faller, D. V., Ngo, D., Lew, R. A., Freeman, J. E., Rogers, A. E., "Medical hyperspectral imaging to facilitate residual tumor identification during surgery," Cancer Biol. Ther. 6, 439-446 (2007).

[10] Boucheron, L., Zhiqianf, B., Harvey, N. R., Manjunath, B. S., Rimm, D. L., "Utility of multispectral imaging for nuclear classification of routine clinical histopathology imagery," BMC Cell Biol. (Suppl. 1) 8, S8 (2007).

[11] Leavesley, S. J., Walters, M., Lopez, C., Baker, T., Favreau, P. F., Rich, T. C., Rider, P. F., Bordeaux, C. W., "Hyperspectral imaging fluorescence excitation scanning for colon cancer detection," J. Biomed. Opt. 21, 104003 (2016).

[12] Masood, K., Rajpoot, N., Rajpoot, K., Qureshi, H., "Hyperspectral colon tissue classification using morphological analysis," in Proc. IEEE Int. Conf. on Emerging Technologies 2016, Peswar, Pakistan, November 13-14, 2016, pp. 735-741.

[13] Maggioni, M., Davis, G., Warner, F. J., Coifman, L. R., "Hyperspecral microscopic analysis of normal, benign and carcinoma microarray tissue sections," in: Proc. SPIE 6091, 60910I (2006).

[14] Masood, K., Rajpoot, N., "Texture based classification of hyperspectral colon biopsy samples using CLBP," in Proc. IEEE Int. Symp. on Biomed. Imaging: From Nano to Micro 2009, 2009, pp. 1011-1014.
[15] Halicek, M., Guolan, L., Little, J. V., Wang, X., Patel, M., Griffith, D., et al., Deep convolutional neural networks for classifying head and neck cancer using hyperspectral imaging, J. Biomed. Opt. Lett. 22, 060503 (2017).
[16] Akbari, H., Halig, L. V., Schuster, D. M., Osnukova, A., Master, V., Nieh, P. T., et al., "Hyperspectral imaging and quantitative analysis for prostate cancer detection," J. Biomed. Opt. 17, 076005 (2012).
[17] Renkoski, T. E., Hatch, K. D., Utzinger, U., "Wide-field spectral imaging of human ovary autofluorescence and oncologic diagnosis via previously collected probe data," J. Biomed. Opt. 17, 036003 (2012).
[18] Isabelle, M., Rogers, K., Stone, N., "Correlation mapping: rapid method for identification of histological features and pathological classification in mid infrared spectroscopic images of lymph nodes," J. Biomed. Opt.15, 026030 (2010).
[19] Keshava, N., Mustard, J. F., "Spectral unmixing," IEEE Sig. Proc. Mag. 19, 44-57 (2002).
[20] Bioucas-Dias, J. M., Plaza, A., Dobigeon, N., Parente, M., Du, Q., Garder, P., Chanussot, J., "Hyperspectral Unmixing Overview: Geometrical, Statistical, and Sparse Regression-Based Approaches," IEEE J. Sel. Top. in Appl. Earth Observation and Remote Sens. 5, 354-379 (2012).
[21] Blais-Ouellette, S., "Method and apparatus for a Bragg grating tunable filter," *US patent* 7557990 (B2), issued July 7, 2009.
[22] Roxbury, D., Jena, P. V., Williams, R. M., Enyedi, B., Niethammer, P., Marcet, S., et al., "Hyperspectral Microscopy of Near-Infrared Fluorescence Enables 17-Chirality Carbon Nanotube Imaging," Sci. Rep. 5, 14167 (2015).
[23] Heinz, D., Chang, C. I., "Fully constrained least squares linear spectral mixture analysis method for material quantification in hyperspectral imagery," IEEE Trans. Geosci. Remote Sens. 39, 529-545 (2001)
[24] Winter, M. E., "N-FINDR: An algorithm for fast autonomous spectral endmember determination in hyperspectral data," Proc. SPIE 3753, 266-277 (1999) .
[25] Nascimento, J. M. P., Bioucas-Dias, J. M., "Vertex component analysis: A fast algorithm to unmix hyperspectral data," IEEE Trans. Geosci. Remote Sens. 43, 898-910 (2005).
[26] Chan, T. H., Ma, W. K., Ambikaphati, A., Chi, C. Y., "A simplex volume maximization framework for hyperspectral endmember extraction," IEEE Trans. Geosci. Remote Sens. 49, 4177-4193 (2011).
[27] Pu, H., Xia, W., Wang, B., Jiang, G. M., "A Fully Constrained Linear Spectral Unmixing Algorithm Based on Distance Geometry," IEEE Trans. Geosci. Remote Sens. 52, 1157-1176 (2014).